J. Phys. Chem. A **2007,** *111,* 3850−3861

Determination of the Rate Constant for the $OH(X^2\Pi) + OH(X^2\Pi) \rightarrow O(^3P) + H_2O$ Reaction over the Temperature Range 293−373 K[†]

Mi-Kyung Bahng and R. Glen Macdonald*

Chemistry Division, Argonne National Laboratory, 9700 South Cass Avenue, Argonne, Illinois 60439-4831

Received: September 27, 2006; In Final Form: December 11, 2006

The rate constant for the reaction $OH(X^2\Pi) + OH(X^2\Pi) \rightarrow O(^3P) + H_2O$ has been measured over the temperature range 293−373 K and pressure range 2.6−7.8 Torr in both Ne and Ar bath gases. The OH radical was created by 193 nm laser photolysis of N_2O to produce $O(^1D)$ atoms that reacted rapidly with H_2O to produce the OH radical. The OH radical was detected by quantitative time-resolved near-infrared absorption spectroscopy using Λ-doublet resolved rotational transitions of the first overtone of OH(2,0) near 1.47 μm. The temporal concentration profiles of OH were simulated using a kinetic model, and rate constants were determined by minimizing the sum of the squares of residuals between the experimental profiles and the model calculations. At 293 K the rate constant for the title reaction was found to be $(2.7 \pm 0.9) \times 10^{-12}$ cm^3 molecule^{-1} s^{-1}, where the uncertainty includes an estimate of both random and systematic errors at the 95% confidence level. The rate constant was measured at 347 and 373 K and found to decrease with increasing temperature.

I. Introduction

The $OH(X^2\Pi)$ radical is a primary oxidant in both combustion and atmospheric chemistry, and as such, its gas-phase chemistry has been widely studied. One of the most interesting reactions involving the OH radical is its self-reaction

$$OH + OH \rightarrow O(^3P) + H_2O \qquad (1a)$$

$$OH + OH + M \rightarrow H_2O_2 + M \qquad (1b)$$

Both reactions 1a and 1b play important roles in combustion chemistry.[1] Both reactions are chain-terminating steps, whereas the reverse reaction of (1a) is chain propagating. Together, reaction 1a and its reverse are responsible for the establishment of pseudo-equilibrium conditions in post-flame conditions.[2] On the other hand, reaction 1b and subsequence oxidation of H_2O_2 can lead to the formation of the HO_2 radical at lower combustion temperatures.[3]

Reaction 1 is also prototypical of radical−radical reactions. These types of reactions are characterized by several unique features.[4] There are always multiple potential energy surfaces (PESs) belonging to different spin manifolds because of the pairing or antipairing of electron spin. Generally, the PES arising from the antiparallel electron spins leads to a bound species without the formation of an activation barrier, such as channel 1b. If one of the species possesses electronic angular momentum, there are also multiple electronic as well as spin manifolds. Reaction 1a is an example of this latter type of radical−radical interaction, and in planar symmetry the reactants correlate to $2(^{1,3}A'' + {}^{1,3}A')$ PESs.

Radical−radical reactions are difficult to study experimentally because, in general, the temporal dependence of the concentration of two transient species must be followed to determine the reaction rate constant. The study of a radical self-reaction reduces this to the necessity of only knowing the concentration of a single transient species.

Reaction 1 has been one of the most widely studied radical−radical reactions. Many of the experimental measurements have been directed at the determination of the rate constant for reaction 1a, k_{1a}, near room temperature. There have been at least 13 measurements[5−17] of k_{1a} near 300 K; however, only three of these studies[15,16,17] explored the temperature dependence of the rate constant. Even though there are a large number of measurements for k_{1a}, there is considerable uncertainty in its value at 300 K. The measurements span the range from 0.85×10^{-13} to 2.57×10^{-12} cm^3 molecule^{-1} s.$^{-1}$ A number of techniques have been used to determine k_{1a}. Most workers have used the discharge flow (DF) method to generate the OH radical with various methods used to determine the OH concentration: mass spectrometry (MS), electron spin resonance (ESR) spectrometry, and resonance absorption (RA) or resonance emission (RE) spectroscopy. Several workers have used flash photolysis at modest pressures, 20−400 Torr, to generate OH and RA spectroscopy to determine its concentration. A recent IUPAC evaluation[18] selected a few of these measurements to provide a recommended value for k_{1a} of $(1.5 \pm 0.6) \times 10^{-12}$ cm^3 molecule^{-1} s^{-1}, at 298 K, where the uncertainty is at the 95% confidence limit. The two most recent measurements[16,17] of k_{1a} and its temperature dependence near 300 K would appear to confirm the IUPAC evaluation.

The reverse of reaction 1a has been studied at temperatures between 750 and 1045 K using a DF/MS detection scheme.[19] The equilibrium constant for reaction 1a can be used to relate the forward and reverse rate constants. Also, reaction 1a and its reverse have been studied at higher temperatures between 1050 and 2380 K using the shock tube technique. In these studies, the OH radical was monitored by UV laser absorption[20] or the $O(^3P)$ atom was monitored by atomic resonance absorption.[21,22]

The dynamics of reaction 1a in the vicinity of the transition state has been probed experimentally by dissociative photode-

---

[†] Part of the special issue "James A. Miller Festschrift".

* To whom correspondence should be addressed. Fax: (630) 252-9292. E-mail: rgmacdonald@anl.gov.

10.1021/jp066359c CCC: $37.00

tachment spectroscopy of $H_2O_2^-$. Deyerl et al.[23] observed vibrationally resolvable reactant and product vibrational levels in the photoelectron spectrum. These results indicate that the H_2O product of reaction 1a is vibrationally excited, and there is strong vibrational adiabaticity in the system. These workers also calculated optimum geometries and energies of some stationary points on the $^3A''$ PES at the UQCISD(T)/6-311++G-(3df,2p) level of theory.

Reaction 1a has also received considerable theoretical scrutiny. The theoretical challenges are equally difficult for this reaction as the experimental ones. Not only are there multiple PESs belonging to both electronic and spin manifolds, but the long-range nature of the intermolecular forces between two OH radicals is complicated by the presence of both strong hydrogen-bonding and electrostatic forces.[24] Harding and Wagner[25] showed that two electronic PESs of $^3A''$ and $^3A'$ symmetry contributed to the observed reaction rate constant. These workers used variational transition state theory and ab initio electronic structure calculations at the MCSCF/GVB+1+2 level of theory to calculate the temperature dependence of k_{1a} from 300 to 2000 K. They found that the temperature dependence of k_{1a} exhibited a strong non-Arrhenius behavior. Recently, Karkach and Oscherov[26] calculated the stationary points on the multiple PESs associated with the triplet state asymptotes of H_2O_2 using electronic structure calculations at the QCISD(T)/6-311(d,p) level of theory. Braunstein et al.[27] provided a theoretical description of the reverse of reaction 1a based on classical trajectory calculations and PESs constructed from thousands of fixed geometries calculated at the CASSCF+MP2 level of theory. Like Harding and Wagner,[25] these workers also found that multiple electronic PESs contributed to the thermal rate constant.

In the present work, the rate constant for reaction 1a, k_{1a}, was measured at three temperatures, 293, 347 and 373 K. Unlike previous experiments, the reaction was initiated by pulsed-laser photolysis at pressures from 2.6 to 7.8 Torr. The OH radical was created by 193 nm laser photolysis of N_2O to produce $O(^1D)$ atoms, which rapidly reacted with H_2O to produce the OH radical. The temporal dependence of the OH radical was monitored using quantitative near-infrared absorption spectroscopy based on Λ-doublet resolved rotational transitions of the first overtone of OH(2,0). This method produces a clean source of OH radicals and provides a quantitative and sensitive detection scheme. Over the range of OH radical concentrations in the experiments, 8×10^{11} to 4.5×10^{13} molecules cm^{-3}, the signal-to-noise of the temporal concentration profiles varied from 30 to over 800, respectively, and placed tight restrictions on the values of the rate constants that could reproduce the experimental data. A detailed-kinetic model was used to analyze the experimental results. Rate constants were determined by minimizing the sum of the squares of the residuals between simulated and experimental temporal concentration profiles. The general accuracy of the method was verified by measurement of the rate constant for the $OH + H_2 \rightarrow H + H_2O$ reaction at 293 K. Reaction 1a is a second-order reaction, and various sources of error that could influence its accurate determination will be discussed. These include pulse-to-pulse fluctuations in the initial radical concentration and the radical concentration gradient along the photolysis axis.

II. Experimental Section

The experimental apparatus used in this study has been described in detail previously[28,29] so that only a brief description is given here. The transverse flow reactor (TFR) consists of a stainless steel reaction chamber, an inner Teflon box (100 × 100 × 5 cm^3), and two sidearm chambers housing White cell optics. The TFR can be heated to 390 K using a heated recirculating silicon oil bath (Nestlab EX-250HT). Heating tapes are used to heat the sidearm chambers to the temperature of the reaction region. Reported here are the results recorded at three different temperature, 293 ± 2, 347 ± 4, and 373 ± 3 K.

The sample gases are introduced into the TFR reaction vessel from separate vacuum systems using calibrated mass-flow meters (MKS model 0258). The gases used are N_2O (AGA gas, 99.998% purity), Ne (AGA gas, 99.999% purity), Ar (AGA gas, 99.995% purity) and H_2 (Linde gas, 99.9995% purity). A known flow rate of water vapor is admitted to the TFR reaction vessel through a saturated bubbler system. The partial pressure of H_2O in the bubbler is adjusted by the temperature of the water reservoir using a water bath recirculator (Neslab RTE-111). The total flow rates vary from 300 to 600 sccm depending on the total pressure, which varies from 2.6 to 7.8 Torr. The partial pressure of each component is calculated from the individual gas flow rates and the total pressure. The range in pressure for each component is 1.0−5.0 Torr for the inert gas, 0.4−1.2 Torr for N_2O, and 0.4−1.2 for H_2O.

The photolysis laser is an ArF excimer laser (Lambda-Physik Compex 205) operating at 193 nm and a repetition rate of 3 Hz. A fresh gas sample is photolyzed on each laser pulse. The photolysis laser fluence at the entrance window of the reaction chamber is varied from 1 to 28 mJ/cm^2 using the laser power setting and/or fine stainless steel screens. The attenuation of the photolysis laser power through the chamber was generally about 15%.

The probe laser is a continuous-wave external cavity diode laser (EOS Model 2010-ECU, nominal bandwidth ≤5 MHz), which is tunable from 1.46 to 1.49 μm. The wavelength of the diode laser radiation is monitored by a wave meter (Burleigh Model WA-20) with an accuracy of 300 MHz. A Fabry−Perot spectral analyzer (Burleigh SA Plus, FSR = 2 GHz and finesse = 300) is used to ensure the single mode operation of the diode laser and monitor the frequency stability of the probe laser radiation during data collection. The probe laser is carefully tuned to the peak of an OH spectroscopic transition by monitoring the change in the transmitted laser intensity with the aid of a box-car signal averager. The laser frequency is not locked to the molecular transition but its frequency is noted on an oscilloscope displaying a free spectral range of the spectral analyzer on the time axis. If the box-car signal decreases or the laser frequency drifts more than 20 MHz, the data collection is stopped and the laser frequency retuned to the maximum absorption signal. In the present experiments, the OH radical concentration is 8×10^{11} to 4.5×10^{13} molecules cm^{-3}. The low OH concentrations are achieved by attenuating the photolysis laser, but the probe laser frequency is tuned to the OH line center with the photolysis laser at high power.

The photolysis laser and the probe laser beams are overlapped using an ultraviolet UV/IR dichroic mirror, placed at Brewster's angle on the optical axis of the White cell. The other White cell mirror is protected by a ZnS plate also mounted at Brewster's angle on the optical axis. This optic directs part of the UV beam to a power meter (Molectron Model J-50). The base optical path length is defined by the distance between the two optical elements, 139 cm. Usually, the probe laser radiation is passed 12 times through the volume of gas irradiated by the photolysis laser, giving the total optical path length of 16.68 m.

The hydroxyl radical is monitored by the $OH(v' = 2, v'' = 0)$ P_{1f} (4.5) rotational Λ-doublet transition.[30,31] The signal-to-

TABLE 1: Complete Chemical Model Describing the OH + OH Reaction System at 293 K

no.	reactants		products	k (cm^3 molecule^{-1} s^{-1})^{a,b}	ref
1a, R1a	$OH + OH$	→	$H_2O + O$	optimized	this work
1b, R1b	$OH + OH + Ne/Ar$	→	$H_2O_2 + Ne/Ar$	3.7×10^{-31} [M]	32
1c	$OH + OH + H_2$	→	$H_2O_2 + H_2$	3.7×10^{-31} [H$_2$]	32, 33
1d	$OH + OH + N_2O$	→	$H_2O_2 + N_2O$	7.0×10^{-31} [N$_2$O]	33
1e	$OH + OH + H_2O$	→	$H_2O_2 + H_2O$	7.0×10^{-31} [H$_2$O]	33
2, R2	$OH + O(^3P)$	→	$H + O_2$	3.49×10^{-11}	34
3a, R3a	$O(^1D) + H_2O$	→	$OH + OH$	2.2×10^{-10}	34
3b, R3b		→	$H_2 + O_2$	2.2×10^{-12}	34
3c, *R3c*		→	$O(^3P) + H_2O$	4.0×10^{-12}	35
4a	$O(^1D) + N_2O$	→	$NO + NO$	7.2×10^{-11}	36
4b		→	$O_2 + N_2$	4.4×10^{-11}	36
4c		→	$O(^3P) + N_2O$	1.0×10^{-12}	36
5	$O(^1D) + Ne$	→	$O(^3P) + Ne$	1.0×10^{-15}	37
	$O(^1D) + Ar$	→	$O(^3P) + Ar$	8.0×10^{-13}	38
6a	$O(^1D) + H_2$	→	$OH + H$	1.1×10^{-10}	34
6b		→	$O(^3P) + H_2$	5.4×10^{-12}	35
7	$OH + H_2$	→	$H_2O + H$	6.09×10^{-15}	34
8	$OH + H_2O_2$	→	$H_2O + HO_2$	1.80×10^{-12}	34
9	$OH + HO_2$	→	$H_2O + O_2$	9.9×10^{-11}	39
10	$HO_2 + NO$	→	$OH + NO_2$	8.0×10^{-12}	40
11a	$OH{+}H + Ne/Ar$	→	$H_2O + Ne/Ar$	2.7×10^{-31} [M]	41
11b	$OH + H + H_2$	→	$H_2O + H_2$	2.7×10^{-31} [H$_2$]	41
11c	$OH + H + N_2O$	→	$H_2O + N_2O$	7.1×10^{-31} [N$_2$O]	41
11d	$OH + H + H_2O$	→	$H_2O + H_2O$	4.5×10^{-30} [H$_2$O]	41
12a	$OH + NO + Ne/Ar$	→	$HONO + Ne/Ar$	7.8×10^{-31} [M]	18, 42
12b	$OH + NO + H_2$	→	$HONO + H_2$	7.8×10^{-31} [H$_2$]	18
12c	$OH + NO + N_2O$	→	$HONO + N_2O$	7.8×10^{-31} [N$_2$O]	18
12d	$OH + NO + H_2O$	→	$HONO + H_2O$	3.9×10^{-30} [H$_2$O]	18^c
13	X	→	X (diffusion)	optimized	see text

^{a} Second-order rate constants units in cm^3 molecule^{-1} s.$^{-1}$ ^{b} Third-order rate constants units in cm^6 molecule^{-2} s.$^{-1}$ For recombination reactions, the falloff region was accounted for using simplified parameters, k_0, k_∞, and F_c. ^{c} H_2O taken as 5 times more efficient than N_2.

noise of the absorbance measurement is increased using a differential detection scheme. The probe laser beam is split into two beams; each is monitored by identical InGaAs detectors (New Focus Model 2053). The signals from both detectors are equalized using linear polarizers and are sent to a differential amplifier (Oregon Analog Tools Model 7A13). Unnecessary electronic bandwidth can be reduced using a multichannel electronic filter (Krohn-Hite Model 3944). The difference signals are recorded and signal-averaged using a digital oscilloscope (LeCroy Model 9410). The initial probe laser intensity (I_0) is recorded using a boxcar (Stanford Research Model 250) that is triggered 0.3 ms prior to the photolysis laser. Thermal lensing and refractive index changes in the optical elements exposed to the excimer laser result in oscillations superimposed on the absorption signal. These unwanted features are removed by recording a background profile with the probe laser tuned to a zero-absorption region and subtracting the two traces. Data collection is controlled by a PC computer.

III. Results and Discussion

A. Reaction Mechanism. The reaction sequence is initiated by the 193 nm photolysis of N_2O to create $O(^1D)$ atoms, and the rapid reaction of $O(^1D)$ with H_2O to generate the OH radical. The complete reaction model[32−42] is given in Table 1; however, the following reactions account for over 95% of the chemistry involving the OH radical:

$$N_2O \xrightarrow{193\text{ nm}} N_2 + O(^1D)$$

$$O(^1D) + H_2O \rightarrow OH + OH \qquad \Delta H° = -118.5\text{ kJ/mol} \tag{R3a}$$

$$OH + OH \rightarrow O(^3P) + H_2O \qquad \Delta H° = -67.2\text{ kJ/mol} \tag{R1a}$$

$$OH + OH + M \rightarrow H_2O_2 + M \qquad \Delta H° = -210.9\text{ kJ/mol} \tag{R1b}$$

$$OH + O \rightarrow H + O_2 \qquad \Delta H° = -68.5\text{ kJ/mol} \tag{R2}$$

$$OH \rightarrow \text{diffusion} \tag{13}$$

Recently, the yield of $O(^3P)$ atoms from the 193 nm photolysis of N_2O has been shown[43] to be 0.5% and was neglected in the model calculations. Electronic quenching of $O(^1D)$ is an additional source of the $O(^3P)$ production, besides reaction 1a. Although this contribution is minor, recent experiments[44−46] have indicated slightly different values than given in Table 1 for reactions 3c and 4c, and will be discussed in section III.H. Under the low-pressure conditions of the experiment, 2.6−7.6 Torr, the contribution of reaction 1b to the removal of OH is small; at the highest pressures, the effective second-order rate constant is about 1×10^{-13} cm^3 molecule^{-1} s^{-1}.

We note that the reaction enthalpies at 298 K shown above were calculated on the basis of the most recent thermodynamic values given by Ruscic et al.[47,48] Table 2 summarizes the enthalpies[36,49,50] of the species in the OH + OH reaction model.

As will be discussed in section III.E, the removal of OH by diffusion can account for over 50% of the removal of OH, and the treatment of diffusion deserves special comment. The binary diffusion constant, D_{12}^{X}, for each species in the reaction model was calculated by the method of Fuller et al.,[51,52] as discussed recently,[53] and the binary diffusion constant for the mixture was calculated using mole fraction weighted binary diffusion constants. For the H atom, the diffusion volume was adjusted to match the experimental measurements for D_{12}^{H} by Lynch and Michael.[54] The determination of the diffusional rate constant, k_{diff}^{X}, is complicated by the experimental geometry. As in other measurements made in the TFR apparatus,[28,29,53] k_{diff}^{X} is de-

TABLE 2: Summary of the $\Delta H^\circ_f(X)$ of the Species in the OH + OH Reaction Model in Table 1

species	$\Delta H^\circ_{f,298}(X)$ (kJ mol^{-1})	$\Delta H^\circ_{f,0}(X)$ (kJ mol^{-1})	ref
OH	37.30 (±0.30)	37.00 (±0.30)	47
O (^{1}D)	438.9	436.6	49
O (^{3}P)	249.229 (±0.002)	246.844 (±0.002)	48
H	217.9978 (±0.0001)	216.034 (±0.0001)	48
H_2	0	0	
N_2	0	0	
O_2	0	0	
N_2O	82.05	85.500	36
NO	91.04 (±0.08)	90.54 (±0.08)	50
Ne	0	0	
H_2O	−241.818 (±0.033)	−238.916 (±0.033)	47
H_2O_2	−135.8 (±0.2)	−129.7 (±0.2)	50
HO_2	12.3 (±0.08)	15.2 (±0.08)	50
NO_2	33.97 (±0.08)	36.78 (±0.08)	50
HONO	−79.5	−74	36

scribed by a double exponential decay, with the two exponential rates differing by about an order of magnitude. However, in the model calculations diffusion is treated as a simple first-order loss process. Thus, uncertainty is introduced into the description of diffusion by fitting a biexponential decay profile to a single-exponential decay term.

B. Measurement of the Absolute Concentration of the OH Radical. In the present experiments, the bandwidth of the probe laser (fwhm < 5 MHz) is much narrower than the line width of a Doppler-broadened spectral feature. The absorbance at frequency ν, $A(\nu)$, is given by the Beer−Lambert law:[55]

$$A(\nu) = \ln(I_0(\nu)/I(\nu)) = l\sigma(\nu)[OH] \qquad (E1)$$

where $I_0(\nu)$ and $I(\nu)$ are the incident and transmitted light intensity, respectively, l is the path length, $\sigma(\nu)$ is the absorption cross section at ν, and [OH] is the concentration of OH. The absorption cross section is related to the line strength of the transition j ← i, S_{ij}, by the line shape function $g(\nu)$, $\sigma(\nu) = S_{ij}\, g(\nu)$. At the maximum of a Doppler-broadened absorption feature, the peak absorption cross section, $\sigma(\nu)_{pk}$ is given by the product of the peak of the normalized line shape function for a Doppler profile times the line strength.

In the current experiment, the OH radical was probed on several P branch Λ-doublet transitions of the first OH(2,0) overtone transition. Almost all the data were collected using the OH(2,0) $P_f(4.5)$ transition with a $\sigma_{pk} = (2.73 \pm 0.19) \times 10^{-19}$ cm^3 molecule^{-1} s^{-1} at 293 K, where the uncertainty is at the 95% confidence limit.[56−58]

The initial vibrational state distribution of OH, created in reaction 3, has been investigated by several workers[59,60] to be 0.67:0.18:0.15 for $v = 0$, 1, and 2, respectively. Nonetheless, the excited vibrational states of OH are rapidly quenched by collisions with H_2O and do not influence the determination of k_{1a}. Figure 1a shows the temporal concentration profile for OH($v = 1$), monitoring the OH(3,1) $R_e(3.5)$ Λ-doublet rotational transition, and Figure 1b shows that for OH($v = 0$) under the same experimental conditions. The solid line in Figure 1b is the simulated OH profile using the optimized fit for k_{1a}, as discussed in the following section. Vibrational relaxation of OH($v = 1$) occurs very rapidly, and the OH has essentially equilibrated in a few microseconds. Note that the ratio of the peak concentrations of OH($v = 1$) and OH($v = 0$) in Figure 1 is consistent with the initial vibrational state distribution. The measured vibrational relaxation rate constants for OH($v = 1$) were in reasonable agreement with previous measurements.[61,62]

C. Determination of k_{1a}. As in previous work,[29,53] the chemical equations described by the model in Table 1 were integrated to generate OH temporal concentration profiles. The optimum value for k_{1a} was found by minimizing the sum of the squares of the residuals between the simulated profile and the experimental one. As discussed in section III.A, the diffusional loss process was treated as a first-order process using calculated D_{12}^X values. A geometric factor, Geom, relates D_{12}^X values to rate constants by $k_{diff}^X = D_{12}^X$ Geom. This factor was determined by measuring k_{diff}^{OH} from OH temporal concentration profiles obtained at attenuated photolysis laser powers, but under identical experimental conditions used to evaluate k_{1a}. The value of k_{diff}^{OH} was determined from the average of several measurements at low OH concentrations for each experimental run. At OH concentrations less than 2×10^{12} molecules cm^3, diffusion accounts for over 90% of the removal of OH (see section III.E), and the simulated OH profiles are insensitive to the value of k_{1a} used to calculate them. For example, k_{1a} was varied from 1×10^{-13} to 4×10^{-12} cm^{-3} molecule^{-1} s^{-1}, but the change in k_{diff}^{OH} was always less than ±5%, about a factor of 2 smaller than the uncertainty in the final value of k_{diff}^{OH} determined from the fitting procedure at the 68% goodness-of-fit confidence level. For each experimental run, the final value of k_{diff}^{OH} was evaluated with k_{1a} equal to the values measured in this work.

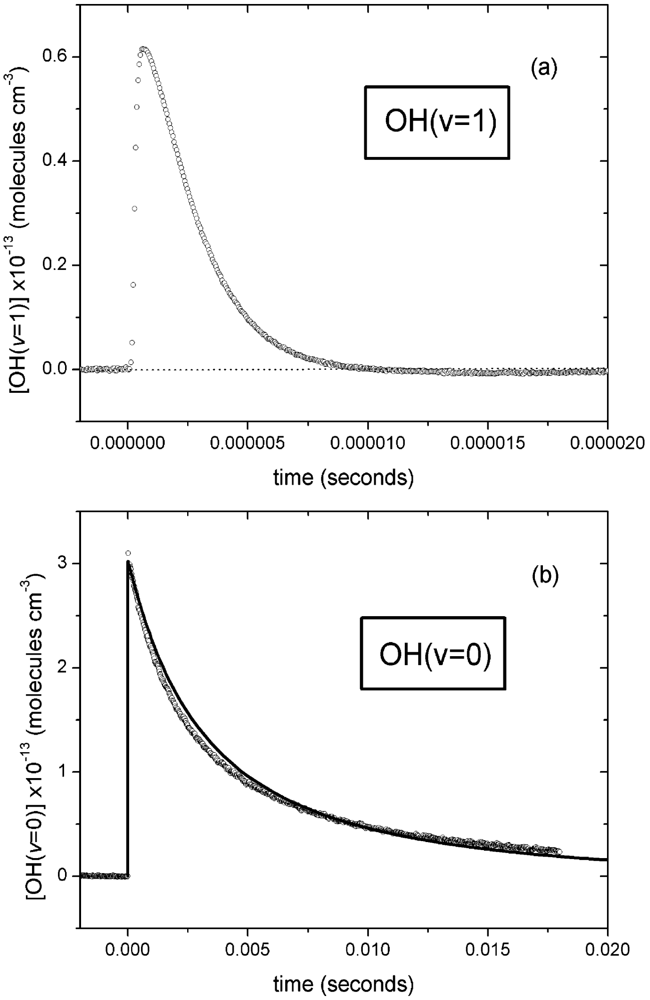

Figure 1. (a) Experimental temporal concentration profile for OH($v = 1$) shown by the circles (○). The conditions of the experiment were $P_{Ne} = 3.10$, $P_{N_2O} = 0.617$, and $P_{H_2O} = 0.741$ Torr at 294 K. The measured vibrational relaxation rate constant for H_2O was 2.0×10^{-11} cm^3 molecule^{-1} s.$^{-1}$ (b) Same experimental conditions as in (a) but for OH($v = 0$). The experimental data are the circles (○) and the solid line is the optimum fit for k_{1a}, as will be discussed in section III.C. The value found for k_{1a} was $(2.7 \pm 0.6) \times 10^{-12}$ cm^3 molecule^{-1} s^{-1}.

Parts a and b of Figure 2 are a pair of typical experimental temporal OH concentration profiles obtained at a high and low, OH concentration, respectively. These figures illustrate the determination of k_{1a} and $k_{\mathrm{diff}}^{\mathrm{OH}}$. In each panel, the open circles (○) are the experimental data, and the solid lines are the optimum values for k_{1a} and $k_{\mathrm{diff}}^{\mathrm{OH}}$. An advantage of a pulsed-laser initiated experiment is the ability to increase the signal-to-noise level by signal avaeraging. Using the root-mean-square noise of the baseline as a measure of the noise on the absorbance traces and the initial absorbance the signal, the signal-to-noise of the temporal OH profiles in Figure 2a,b are 800 and 40, respectively. This high signal-to-noise ratio, especially, at high OH concentrations is a stringent restriction on the values of k_{1a} that are compatible with the observed OH profiles. The dashed lines in Figure 2a,b show the extent of the model OH profiles calculated using rate constants at the 95% confidence limits in the goodness-of-fit, i.e., $k_{1a} \pm 2\sigma$, and $k_{\mathrm{diff}}^{\mathrm{OH}} \pm 2\sigma$, respectively, where σ is the uncertainty in the fit at the 68% goodness-of-fit level. Note, in Figure 2a, the experimental profile has a characteristic second-order profile, with a long approach to the baseline, whereas in Figure 2b the experimental OH profile is described by a biexponential decay. However, in the model calculations the OH decay is dominated by single-exponential behavior. Hence, a compromise is necessary to fit to the data over the time scale of the experiment. If the data were fit over a short time span, 5 ms, the trend was for $k_{\mathrm{diff}}^{\mathrm{OH}}$ to be larger and k_{1a} to be smaller, respectively and vice versa if the time span was long, 50 ms. However, the effect was small, less than 10% and within the uncertainty in $k_{\mathrm{diff}}^{\mathrm{OH}}$. The 20 ms time span was taken as a compromise.

The determination of k_{1a} was made in two different carrier gases, Ar and Ne, to vary the conditions of the experiment. With Ar as the bath gas, diffusion is slower than with Ne; hence, diffusion makes a smaller contribution to the removal of OH in Ar. However, the use of Ar increases the O(^{3}P) concentration by electronic quenching of O(^{1}D), and hence, increases the removal of OH by reaction 2 (see Table 1). Tables 3 and 4 summarize the 293 K experimental conditions and the values of k_{1a} determined with Ar and Ne as carrier gas, respectively. The values of k_{1a} shown in Tables 3 and 4 are the average of 2−5 determinations with different initial OH concentrations at each total pressure. The average k_{1a} values for each carrier gas are shown at the bottom of Tables 3 and 4. With Ar as the carrier gas, k_{1a} was $(2.61 \pm 0.23) \times 10^{-12}$ cm^3 molecule^{-1} s^{-1}, and with Ne, k_{1a} was $(2.80 \pm 0.29) \times 10^{-12}$ cm^3 molecule^{-1} s^{-1}, both at 293 ± 2 K. The quoted uncertainty is the scatter in the data of one standard deviation ($\pm 1\sigma$). There is no statistically significant difference between the Ar and Ne measurements. About an equal number of measurements were made in each bath gas so that k_{1a} was determined to be $(2.70 \pm 0.26) \times 10^{-12}$ cm^3 molecule^{-1} s^{-1} at 293 ± 2 K.

The high-temperature experimental conditions are similar to those in Tables 3 and 4 and are not listed. The values for k_{1a} decreased with increasing temperature. At 347 ± 4 K, k_{1a} in Ar was measured to be $(2.00 \pm 0.32) \times 10^{-12}$ cm^3 molecule^{-1} s^{-1} and in Ne k_{1a} was $(2.02 \pm 0.30) \times 10^{-12}$ cm^3 molecule^{-1} s.$^{-1}$ At 373 ± 3 K, Ar was the only carrier gas used, and k_{1a} was measured to be $(2.24 \pm 0.23) \times 10^{-12}$ cm^3 molecule^{-1} s^{-1}, slightly higher than the value at 347 K.

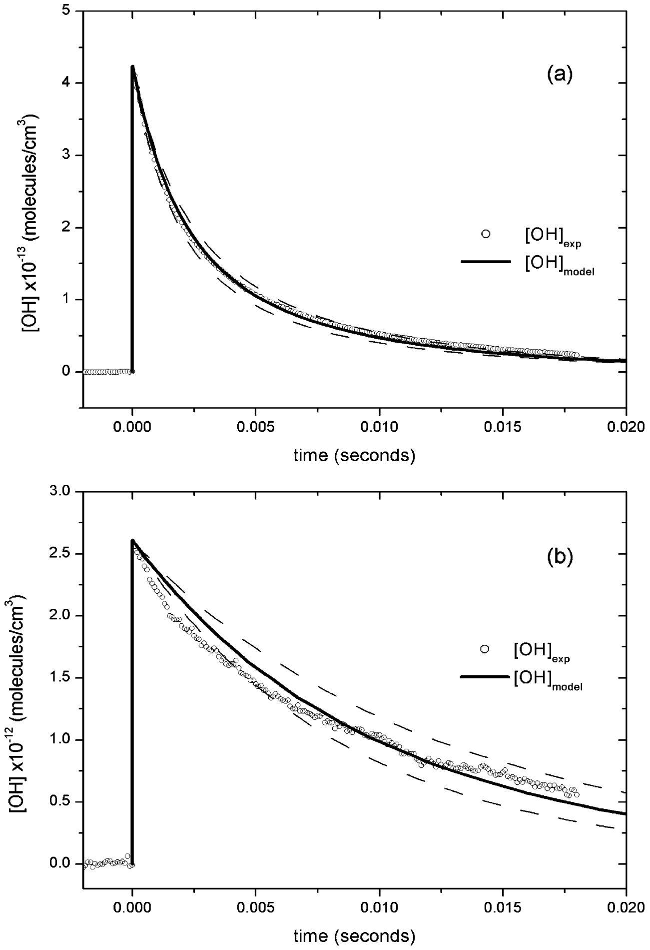

Figure 2. (a) Typical experimental OH temporal concentration profile (○) showing the model OH profile (solid line) calculated using the optimum k_{1a}. The experimental data is shown every 10th point. The optimum value of k_{1a} was $(2.9 \pm 0.6) \times 10^{-12}$ cm^3 molecule^{-1} s^{-1} at the 95% confidence limit. The dashed lines are model calculations showing OH profiles for k_{1a} differing by $\pm 2\sigma$. For this experiment, the ArF fluence was about 24 mJ cm^{-2} and the pressures were $P_{\mathrm{Ne}} =$ 2.94, $P_{\mathrm{N_2O}} = 1.54$, and $P_{\mathrm{H_2O}} = 1.51$ Torr at $T = 293$ K. (b) Similar to (a) except for the determination of $k_{\mathrm{diff}}^{\mathrm{OH}}$ under the same conditions. The solid line is the OH profile calculated using the optimum $k_{\mathrm{diff}}^{\mathrm{OH}} = 85 \pm$ 20 s^{-1} at the 95% confidence level. The dashed lines are the model OH profiles for $k_{\mathrm{diff}}^{\mathrm{OH}}$ differing by $\pm 2\sigma$. The ArF laser fluence was about 1.5 mJ cm.$^{-2}$ Note: the biexponential decay character of the experimental OH profile.

TABLE 3: Summary of Experimental Measurements of k_{1a} in Ar at 293 ± 2 K

P_{total} (Torr)	partial pressure (Torr)			rate constant
	P_{Ar}	$P_{\mathrm{N_2O}}$	$P_{\mathrm{H_2O}}$	$10^{12}k_{1a}$ (cm^3 molecule^{-1} s^{-1})
2.642	1.441	0.571	0.629	2.50 (±0.70)
3.440	2.316	0.579	0.545	3.02 (±0.45)
3.474	2.363	0.582	0.528	2.48 (±0.70)
3.635	2.190	0.387	1.058	2.54(±0.50)
3.747	2.249	0.562	0.936	2.78 (±0.45)
3.787	2.185	0.543	1.059	2.73 (±0.45)
3.789	2.555	0.629	0.604	2.45 (±0.60)
6.874	4.615	1.142	1.117	2.70(±0.39)

$k_{1a} = (2.61 \pm 0.23) \times 10^{-12}$ cm^3 molecule^{-1} s^{-1}

Figures 3 and 4 summarize the results of the measurements of k_{1a} in this work. Figure 3 shows k_{1a} as a function of the initial OH concentration, [OH]$_0$. The solid diamonds represent the values of k_{1a} with Ar as a carrier gas and the solid circles k_{1a} with Ne. The error bars are one standard deviation ($\pm 1\sigma$) in the scatter of the k_{1a} values measured under similar conditions, i.e., [OH]$_0$ within ± 10%. The dotted line shows the average value of k_{1a}. We note that only the measurements for [OH]$_0 >$ 1.0×10^{13} molecules cm^{-3} were included in the determination of k_{1a} because reaction 1a makes a larger contribution to the removal of OH at higher OH concentrations, as addressed in

TABLE 4: Summary of Experimental Measurements of k_{1a} in Ne at 293 ± 2 K

P_{total} (Torr)	partial pressure (Torr) P_{Ne}	P_{N_2O}	P_{H_2O}	rate constant $10^{12}k_{1a}$ (cm^3 $molecule^{-1}$ s^{-1})
3.688	2.263	0.913	0.512	2.66 (±0.72)
3.690	2.235	1.116	0.339	3.15 (±0.85)
3.810	2.223	1.079	0.508	3.02 (±0.64)
4.020	3.009	0.473	0.538	2.87 (±0.84)
4.470	3.063	0.667	0.740	2.75 (±0.60)
5.292	2.483	1.312	1.497	2.62 (±0.39)
5.987	2.935	1.534	1.518	3.14 (±0.32)
7.824	6.234	0.784	0.806	2.55 (±0.45)

$k_{1a} = (2.80 \pm 0.29) \times 10^{-12}$ cm^3 $molecule^{-1}$ s^{-1}

section III.E. In Figure 3b, the symbols are the same as in Figure 3a except the open diamonds (◇) are the measurements of k_{1a} in Ar at 373 ± 3 K. In Figure 3b, the dashed line shows the average value of k_{1a} at 347 K and the dotted line the average value at 373 K. There is little apparent difference between the values of k_{1a} measured at 347 and 373 K, within the stated error bars, as is evident in Figure 3b, although the high-temperature rate constants are clearly smaller than those at a room temperature shown in Figure 3a. This trend is consistent with the observation of small negative temperature dependence for k_{1a} found by Bedjanian et al.[16] from 233 to 360 K and by Sun et al.[17] from 220 to 320 K. The recent recommendation for k_{1a} by the IUPAC subcommittee[18] suggests the modified Arrhenius expression of $k_{1a} = 6.2 \times 10^{-14}(T/298)^{2.6} \exp(945/T)$ cm^3 $molecule^{-1}$ s^{-1} from 200−350 K.

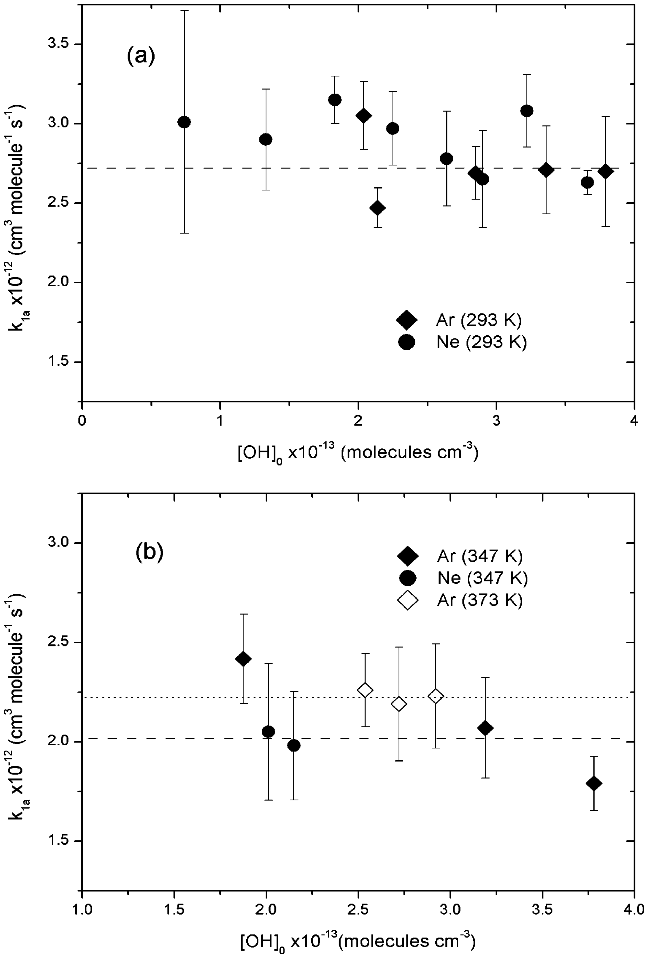

Figure 3. (a) Optimized rate constant k_{1a} as a function of the initial OH concentration at 293 K in different carrier gases, Ar shown by the diamonds (◆) and Ne by the circles (●). The dashed line is the average value of $k_{1a} = 2.7 \times 10^{-12}$ cm^3 $molecule^{-1}$ s^{-1}. (b) Same as (a) except at 347 and 373 K. The dashed line is the average value of $k_{1a} = 2.0 \times 10^{-12}$ cm^3 $molecule^{-1}$ s^{-1} at 347 K, and the dotted line is the average value of $k_{1a} = 2.2 \times 10^{-12}$ cm^3 $molecule^{-1}$ s^{-1} at 373 K.

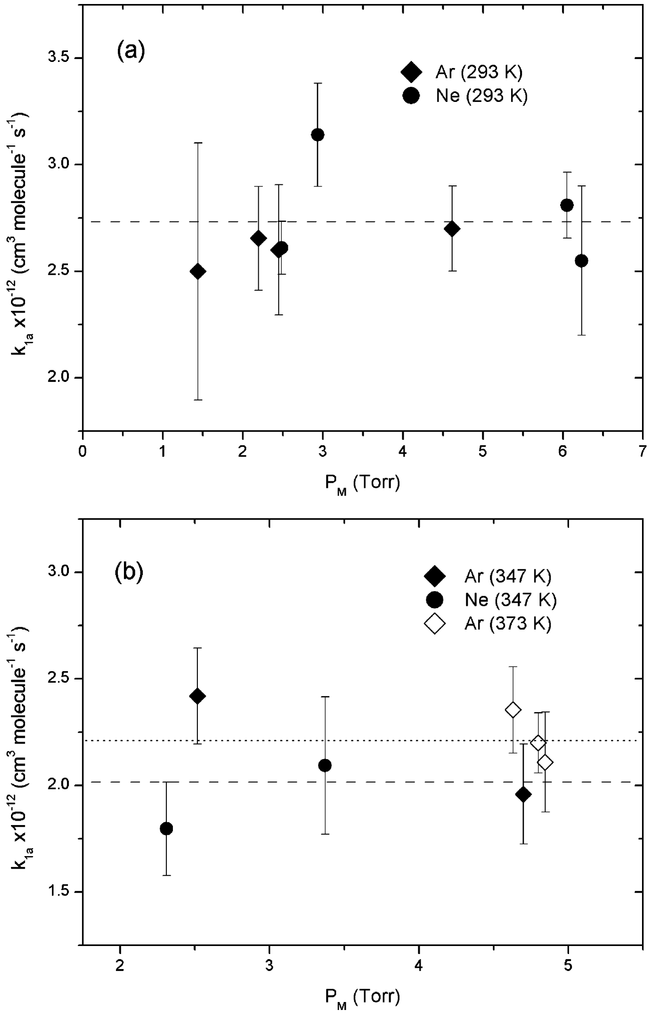

Figure 4. (a) Same as Figure 3 except k_{1a} as a function of the initial pressure of carrier gases at 293 K, Ar shown by the solid diamonds (◆) and Ne by the circles (●). (b) Same as (a) except at 347 and 373 K. The open diamonds (◇) are for Ar carrier gas at 373 K. The dashed and dotted lines are the same average values as in Figure 3.

Figure 4 shows the results for the measurement of k_{1a} as a function of the partial pressure of the carrier gas, either Ar or Ne. The symbols are the same as in Figure 3. It is clear from Figure 4a,b that k_{1a} is independent of the nature of the carrier gas and its partial pressure at all temperatures.

D. Experiments with H_2. As will be discussed in section III.G, the measured values for k_{1a} determined in this work are significantly higher than most of the previously reported values. Therefore, as a way of verifying our experimental technique, we made two different types of measurements involving the $OH + H_2$ reaction. First, we measured k_{1a} in gas mixtures with a small partial pressure of H_2 added to the gas flow. Under these conditions, the $OH + H_2 \rightarrow H + H_2O$, reaction 7 in Table 1, dominates over the slow exponential diffusional rate constant, and the OH decay has a more first-order decay appearance. Second, we measured the well-characterized rate constant for reaction 7, under conditions similar to those for the measurements for k_{1a}, in Tables 3 and 4.

Typical OH temporal concentration profiles of these two types of experiments are shown in Figure 5. In Figure 5a, the long

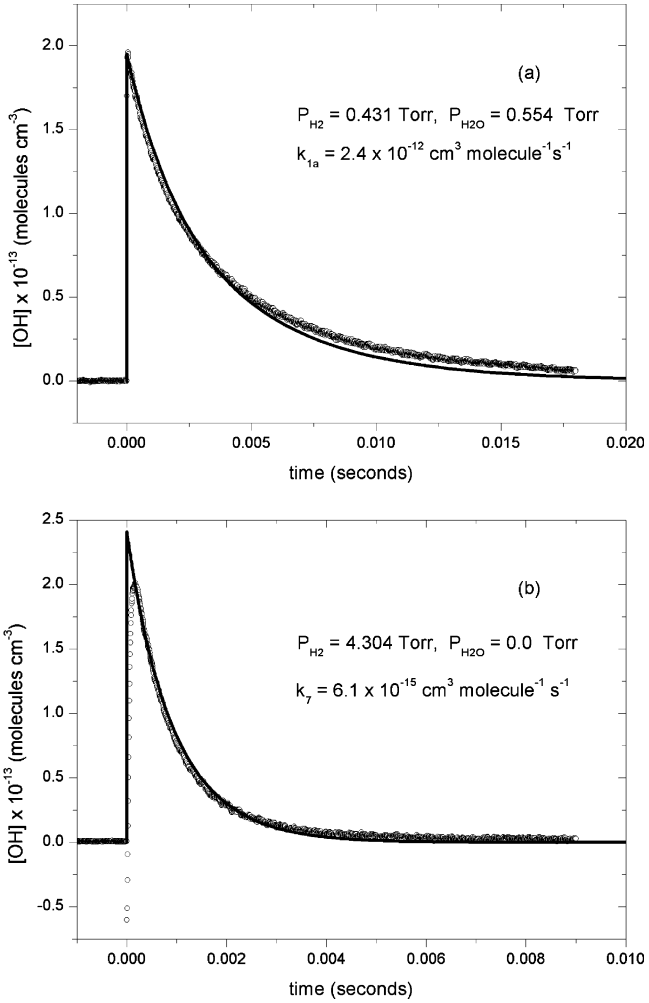

Figure 5. (a) Typical OH concentration profile with a low partial pressure of H_2 in $Ar/H_2O/N_2O/H_2$ mixtures. The open circles (○) are the experimental data points and the solid line the OH profile generated with the optimum value of k_{1a}. Reaction 7 suppresses the influence of the smaller OH diffusional rate constant (see text). The conditions of the experiment were $P_{Ar} = 1.90$, $P_{H_2O} = 0.554$, $P_{N_2O} = 0.507$, and $P_{H_2} = 0.431$ Torr at 293 K. (b) Typical OH concentration profile in H_2/N_2O mixtures to measure k_7, $OH + H_2 \rightarrow H + H_2O$. The open circles (○) are the experimental data points, and the solid line the OH profile generated with the optimum value of k_7. The negative transient is due to a population inversion between OH($v = 2$) and OH($v = 0$). The conditions of the experiment were $P_{H_2} = 4.30$ and $P_{N_2O} = 0.912$ Torr at 294 K.

time OH decay is dominated by reaction 7, and the OH profile appears more exponential-like compared to the profile in Figure 2a. Unfortunately, the removal flux of OH by reaction 7 was more than by reaction 1a, and consequently, the measurements of k_{1a} were more scattered. The results of seven measurements gave k_{1a} equal to $(2.8 \pm 0.6) \times 10^{-12}$ cm^3 $molecule^{-1}$ s^{-1} at 293 K, where the uncertainty is $\pm 1\sigma$ in the scatter in the data. In Figure 5b, a typical OH temporal concentration profile is shown for mixtures of H_2 and N_2O. At high partial pressures of H_2, reaction 7 accounts for over 90% of the removal flux of OH. Note the large negative spike just after the photolysis laser pulse illustrates the initial population inversion[63] between OH($v = 0$) and OH($v = 2$) created in reaction 6a. The rate constant for reaction 7 was determined using the model in Table 1. Although the reaction conditions were almost first-order and the resulting rate constant measurement not dramatically dependent on the concentration of OH, the model did account for secondary chemistry in the system. If the decay of OH were treated as a pseudo-first-order process, the value of k_7 would have been 7.4×10^{-15} cm^3 $molecule^{-1}$ s^{-1} instead of the optimized value of 6.1×10^{-15} cm^3 $molecule^{-1}$ s^{-1}. In seven separate experiments, the rate constant of the $OH + H_2$ reaction was measured to be $(6.00 \pm 0.48) \times 10^{-15}$ cm^3 $molecule^{-1}$ s^{-1}, where the uncertainty is $\pm 1\sigma$, at 293 ± 1 K. According to the recent measurements of Orkin et al.,[64] k_7 is $(5.95 \pm 0.08) \times 10^{-15}$ cm^3 $molecule^{-1}$ s^{-1} at 293 K.

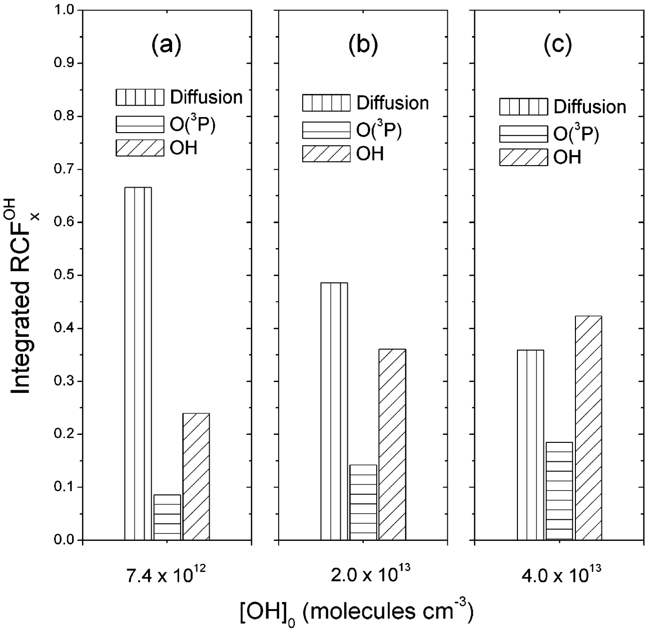

Figure 6. (a) Integrated reaction contribution factors of OH, $IRCF^{OH}_X$ (X = OH, O, and diffusion) at $[OH]_0 = 7.4 \times 10^{12}$ molecules $cm.^{-3}$ (b) Same as (a) except $[OH]_0 = 2.0 \times 10^{13}$ molecules $cm.^{-3}$ (c) Same as (a) except $[OH]_0 = 4.0 \times 10^{13}$ molecules $cm.^{-3}$

The experiments with added H_2 to the gas flow indicated the procedures outlined in sections III.B and III.C are valid. At low partial pressures of H_2, the values of k_{1a} were in agreement with those without H_2, indicating that the determination of k^{OH}_{diff} was reliable (see Figure 5a). At high partial pressures of H_2, the value of k_7 obtained using the model in Table 1 was in good agreement with a recent measurement,[64] again indicating the validity of the reaction model Table 1 (see Figure 5b).

E. Reaction Contribution Factor Analysis. It is crucial to know the influence of each individual reaction in the reaction model on an experimental observation to fully understand a reaction system involving many species and reactions. In the present study, a reaction contribution factor analysis[65] was carried out to determine the contribution of each reaction to the removal of OH. The reaction contribution factor (RCF) at time *t*, for species i removed by reaction with species j, $RCF^i_j(t)$, is given by $RCF^i_j(t) = -k_{ij}[i][j]$. Similarly, for species i produced by reaction between species l and m, it is given by $RCF^i_{lm}(t) = k_{lm}[l][m]$. The corresponding integrated RCF, $IRCF^i_{j/lm}$, from $t = 0$ to time *t*, is the total flux of species i that is removed in reaction with j or produced in reaction between l and m, respectively, up to time *t*. This is often called the reaction pathway contribution. The $RCF^{OH}_X(t)$ and $IRCF^{OH}_X$ for each species X in the model were calculated in each determination of k_{1a}. Figure 6 shows the results of the reaction contribution analysis for OH removal at three different initial OH radical concentrations. As mentioned in section III.A, the three major contributions to the removal of OH are reactions 1a and 2 and diffusion. They account for more than 95% of the removal processes for OH. Figure 6a shows the $IRCF^{OH}_X$'s for these reactions at an initial concentrations of OH of 7.4×10^{12} molecules cm.$^{-3}$ As expected, the diffusional loss is the dominant source of OH consumption at this low initial OH concentration. Figure 6b shows the same IRCF_X^{OH}'s for an initial concentration of OH of 2.0×10^{13} molecules cm,$^{-3}$ and Figure 6c shows them for an initial concentration of OH of 4.0×10^{13} molecules cm.$^{-3}$ As expected, diffusional loss dominates for OH removal at the low initial concentrations but is still significant at the higher OH concentration, accounting for 36% of the OH removal for an OH concentration of 4.0×10^{13} molecules cm.$^{-3}$

F. Factors Influencing Second-Order Decay Kinetics. We address two issues that could influence the determination of k_{1a}; both issues result from the evaluation of a second-order rate constant from a signal-averaged concentration profile. First, shot-to-shot power fluctuations of the photolysis laser produce fluctuating initial OH radical concentrations. The determination of k_{1a} depends on the OH concentration, but its evaluation was based on a signal-averaged OH profile. Signal averaging can be used to improve the signal-to-noise in an experiment without error only if the averaged signal is reproducible on a shot-to-shot basis or has a pure exponential decay. Such was not the case for the OH concentration profiles recorded in this work as the OH decay had both first- and second-order components. Second, the initial OH concentration was not constant along the optical axis but decayed exponentially because of the absorption of the photolysis laser radiation by N_2O. Thus, at each instant in time, the probe laser absorption actually measured the absorbance integral, $\int[OH(t,x)]\,dx$, where x is a position along the optical axis, rather than the separation into a simple product of concentration times total path length, $[OH(t)] \times l$, as assumed in the data analysis based on equation E1.

The first situation has been studied by Tulloch et al.[66] From computer simulations describing a first-order build-up and first- and second-order decay of a reaction product, they concluded that as long as the fluctuations in the initial radical concentration was less than ±5% and a sufficient number of averages were accumulated (>32), the error introduced by signal averaging was less than 0.5%. In the current work, the pulse-to-pulse fluctuations of the photolysis laser was less than 5%, and generally 1000 traces were accumulated so that the fluctuations in the initial OH radical concentration had little influence on the results.

The second situation is more complex and model simulations of the experiment were conducted to estimate the effect of the radical concentration gradient along the optical axis. As noted in sections III.A and III.E, reactions 1−3 account for most of the chemistry in the OH + OH reaction scheme. In fact, if the steady-state approximation is applied to the oxygen atom the simple reaction scheme can be directly integrated to give the OH concentration as a function of time, $[OH(t)]$, as

$$[OH](t) = \frac{k_{diff}^{OH}[OH]_0}{(3k_{1a} + k_{diff}^{OH})e^{k_{diff}^{OH}t} - 3k_{1a}} \qquad (E2)$$

where $[OH]_0$ is the initial OH concentration. The influence of the OH concentration gradient along the probed laser beam axis on the measured k_{1a} values can be determined by modeling the observed absorption signal. The absorbance integral, $\int[OH(t,x)]\,dx$, was evaluated by dividing the optical axis into a number of steps, x. At each step, the initial concentration of OH, $[OH(0,x)]$, was calculated from the attenuation of the photolysis laser over that step interval, and at each step the temporal dependence of $[OH(t,x)]$ was calculated using equation E2. The simulation of an effective experimental OH concentration profile, $[OH(t)]$, was generated by summing over the number of steps and dividing by the path length. This simulated OH profile was analyzed using a modified model of the reaction scheme in Table 1 to find the value for k_{1a} that fit the simulated profile to compare with the values used in deriving it. In this modified reaction scheme, quenching of $O(^1D)$ to $O(^3P)$ was neglected because this process was not included in deriving equation E2. In all cases, the simulated values of k_{1a} were within a few percent of the generating values. If the OH concentration depends linearly on x, the absorbance integral can be separated into an OH concentration factor, the average value of OH along the optical path and the path length. The more the OH concentration gradient along the optical axis deviates from linearity the more the value of k_{1a} determined in the data analysis underestimates the true value. For example, an OH gradient of 50%, $P_{N_2O} = 2.3$ Torr, underestimated the value of k_{1a} by about 7%. Although this is a systematic effect, the error is well within the scatter of the measurements.

An example of the influence of the OH concentration gradient on the evaluation of k_{1a} is shown in Figure 7. The experimental OH profile, given by the open circles (○) in Figure 7a,c, was simulated by the procedure just discussed, and by adjusting the initial photolysis energy in the simulation until the initial OH concentration, given by $k_{diff}^{OH}\int[OH(0,x)]\,dx/139$, matched the experimental value. Also shown in Figure 7a are the calculated OH profiles at the start of the photolysis region, $x = 0$ (□), at the end of the photolysis region, $x = 139$ (△), and the average OH concentration profile, $k_{diff}^{OH}\int[OH(t,x)]\,dx/139$, by the line. Panel 7b shows that at this degree of photolysis laser attenuation, −31%, the $OH(0,x)$ concentration still decayed nearly linearly along the path length. Figure 7c shows the result of fitting the simulated OH profile using the computer analysis that determined the rate constants for reaction 1a. The computer analysis of the simulated OH profile returned a value of k_{1a} that was 2% smaller than the value used to generate the simulation profile. Although the OH concentration gradient could cause the measured rate constant to be systematically underestimated, for the gradients used in this work, <35%, the maximum deviation was less than −3%, and was well within the uncertainty in the determination of the optimum value of k_{1a} by the least-squares minimization procedure.

G. Comparison with Previous Works. Figure 8 shows the results of this work and previous measurements of k_{1a} in the temperature region around 300 K. As is evident from Figure 8, there is considerable scatter in the results and even in the temperature dependence of k_{1a}. Only results considered in the IUPAC evaluation[18] of k_{1a} are plotted except for the results from Trainor and von Rosenberg.[13] These measurements were made in a pressure regime where recombination reaction 1b was important. The other measurements, not plotted, span the same range of values shown in Figure 8. It is noteworthy that the temperature dependence of k_{1a} determined by Wagner and Zellner[15] is opposite to that determined in this work and two recent measurements.[16,17]

As noted in the Introduction, reaction 1a has been studied by a wide variety of techniques, most involving the discharge flow method to generate the OH radicals coupled with some method of determining their concentration. These detection methods ranged from MS,[7,9,10,14,16,17] RA,[5,13,15] RF,[12,14,17] ESR,[6,8,10,11] or a combination of the above-mentioned techniques. A popular method has been DF/MS to establish the initial OH radical concentration and RF to follow its time dependence.[14,17] Bedjanian et al.[16] used the DF/MS technique both to monitor

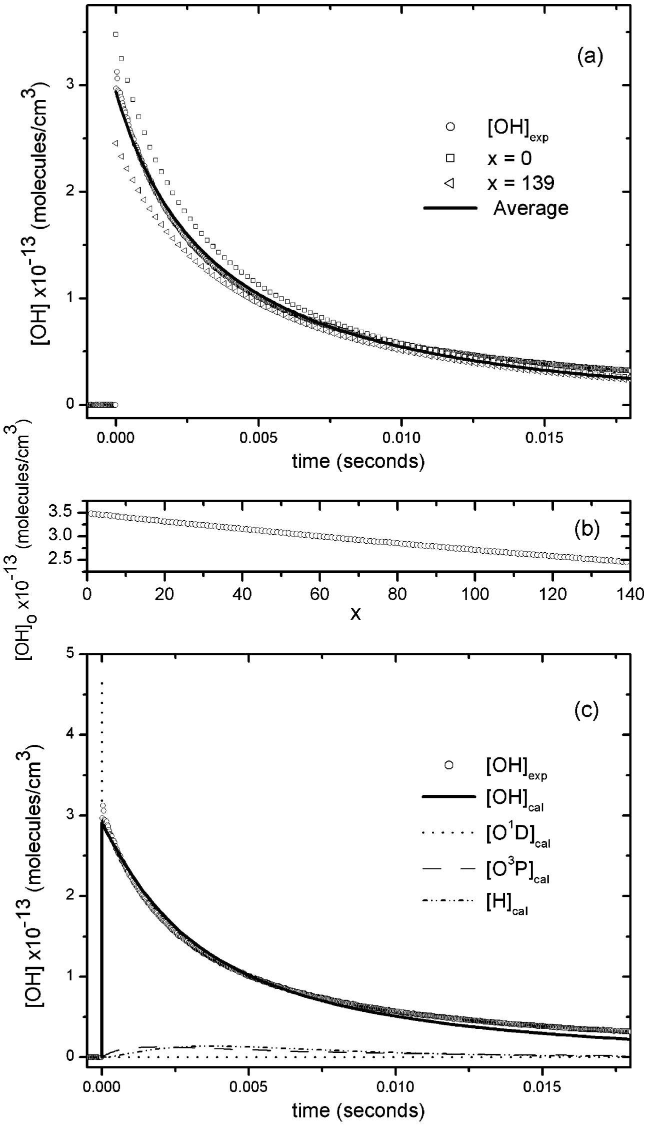

Figure 7. (a) Example of the influence the OH concentration gradient had on the determination of k_{1a}. The OH temporal concentration profile is shown for the initial position at $x = 0$ by the squares (□) and at the final position at $x = 139$ by the triangles (△). The experimental OH profile is shown by the circles (○) and the line is the average integrated absorbance OH profile, as discussed in the text. The conditions of the experiment were $P_{\mathrm{Ar}} = 4.61$, $P_{\mathrm{N_2O}} = 1.14$ and $P_{\mathrm{H_2O}} = 1.12$ Torr at 293 K. For these experimental conditions, k_{1a} was found to be $(2.7 \pm 0.3) \times 10^{-12}$ cm^3 molecule^{-1} s^{-1} and $k_{\mathrm{diff}}^{\mathrm{OH}}$ was 68 ± 7 s^{-1}. (b) [OH(0,x)] gradient along the optical axis. The gradient is close to linear. (c) Analysis of the simulated OH profile, shown in (a). The experimental profile, also shown in (a) is given by the circles (○). The computer calculated profiles of several species are shown by the lines. The reaction mechanism excluded the quenching of O(^{1}D) to O(^{3}P). The computer analysis yielded a value of k_{1a} equal to $(2.65 \pm 0.7) \times 10^{-12}$ cm^3 molecule^{-1} s^{-1}.

the OH time dependence and to provide an absolute concentration measurement. These workers did not monitor OH^+ directly but converted OH to HOBr by the rapid $OH + Br_2 \rightarrow Br + HOBr$ reaction and monitored the $HOBr^+$ ion signal. ESR[6] alone and coupled with MS[10] has been used to monitor the OH concentration. A feature of the ESR technique is the signal depends on the permanent dipole moment; however, it must be calibrated by comparison with a signal from a stable species such as NO.[67] The $H + NO_2 \rightarrow OH + NO$ is a convenient reaction as long as there are no losses of OH in the ESR cavity. As can be seen from Figure 8, the results of the ESR based

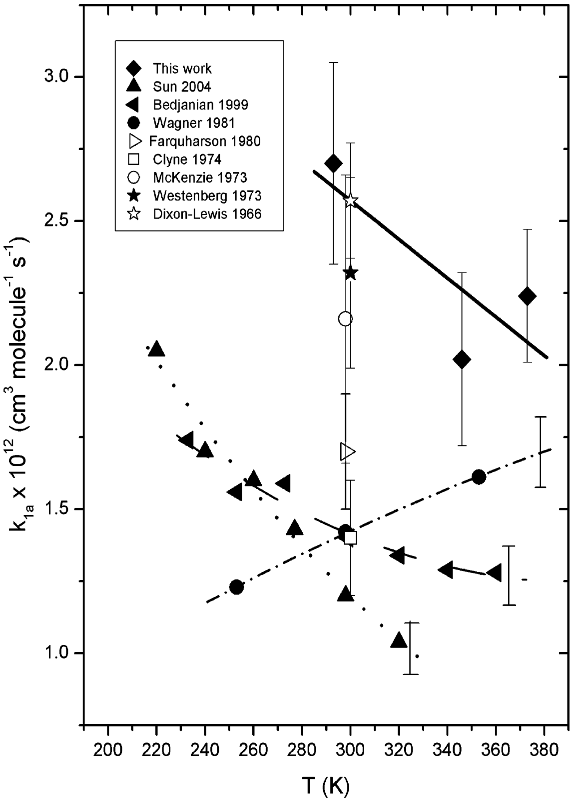

Figure 8. Low-temperature dependence of selected measurements of the rate constant, k_{1a}, for the $OH + OH \rightarrow O(^3P) + H_2O$ reaction. The results of this work (◆) are shown with previous results: Sun and Li[17] (▲); Bedjanian et al.[16] (left solid triangle); Wagner and Zellner,[15] (●); Farquharson and Smith,[14] (△); Clyne and Down,[12] (□); McKenzie et al.,[11] (○); Westenberg and deHaas,[10] (★); Dixon-Lewis et al.,[6] (☆). The uncertainties generally reflect $\pm 1\sigma$ in the scatter in the measurements. The solid lines are fits to the temperature-dependent data. Not shown is a data point at $T = 578$ K, $k_{1a} = 2.1 \times 10^{-12}$ cm^3 molecule^{-1} s^{-1} for the data of Wagner and Zellner.

measurements are in agreement with those of this work near 300 K, within the scatter of the data. A complicating factor in the application of the DF technique is the loss of radicals by wall reaction; thus, the decay is described by first- and second-order rate processes, eq E2. It can be difficult to separate the influence of both processes in the determination of k_{1a}. Two previous studies[13,15] used VUV flash photolysis of H_2O to produce OH and RA to monitor its concentration. However, it was not possible to calibrate the absorption in situ, and it was necessary for these workers to calculate the influence of both Doppler and pressure broadening on the absorption cross section of OH. This makes the determination of the OH concentration more tenuous.

In the current work, pulsed laser photolysis was used to generate the OH radical and tunable-diode laser spectroscopy (TDLS) was used to monitor its concentration. The advantages of this technique are the instantaneous creation of a uniform OH concentration and the straightforward calculation of OH absorption coefficients using known line strengths and shapes. The disadvantage of this technique is the complicated diffusion kinetics caused by the particular geometric configuration used in these experiments. There have been many discussions in the literature about possible systematic errors associated with the DF technique applied to the study of reaction 1a.[10,11,14,68] One difference in the measurements shown in Figure 8 is that generally, the DF/MS/RF experiments were done at pressures near 1 Torr and in the ESR/MS experiments the pressure ranged from 1 to 3 Torr. The experiments of this work were conducted at pressures ranging from 2.6 to 7.8 Torr (see Tables 3 and 4) with no detectable pressure dependence (see Figure 4). The authors can offer no explanation for the scatter in the numerous determinations of k_{1a} except to note that the measurement of the concentration of a transient species can be a challenging undertaking. The more direct the measurement of the radical concentration the more reliable the outcome.

H. Estimated Uncertainties in the Determination of k_{1a}. The uncertainty in determining the OH concentration can be estimated from the uncertainties in the factors that enter eq E1. The absorption cross sections for the $P_{1e/f}$ branch rotational transitions of the OH(2,0) vibrational overtone can be calculated from the known line strengths and the Doppler line shape function. There have been several refinements[57,58] in the values of the line strengths of the OH(2,0) first overtone rotational transitions without any major deviation from the initial determination,[56] and the original estimate of ±7% at the 95% confidence limit is taken as the uncertainty. The procedure for tuning the probe laser frequency to the center of an OH spectroscopic transition was described in section II. The Doppler width of a molecular spectroscopic transition is directly proportional to the frequency of the transition so that the Doppler width of an OH overtone transition is about twice that of the fundamental. Thus, for a rotational transition in the OH(2,0) band, a frequency variation of ±40 MHz only causes an absorption decrease of 1%. This frequency shift is 6 times the resolution of the monitoring scanning spectral analyzer and readily detectable. Furthermore, errors in tuning the laser frequency to the line center would contribute to scatter in the measurements and not to a systematic error. Similarly, the influence of pressure broadening is reduced because of the larger Doppler width of the overtone as compared to the fundamental. The pressure broadening parameters for OH(2,0) in collisions with Ar, Ne, N_2O and H_2O are not known, but those for OH(1,0) in collisions with Ar, He, O_2 and N_2 have been measured.[69] Applying the OH fundamental pressure broadening parameters to the OH first overtone, we made an estimate of the influence of pressure broadening. At the highest pressure used in this work (see Tables 3 and 4), the σ_{pk} was decreased by about 3%, and at 4 Torr, where most of the data were collected, by about 1.5%. However, the decrease in σ_{pk} due to pressure broadening was smaller than the uncertainty in the σ_{pk} itself and was neglected in estimating the overall uncertainty. It should be noted that multiple scans were made of the line shape of the OH(2,0) $P_{1e/f}(4.5)$ transition, but within the uncertainty of these measurements, about ±10%, no deviation from the Doppler width was detected, as expected under these conditions. The path length was defined by the distance between the two optical elements on the axis of the White cell and the number of passes the probe beam made through the photolysis region. The accuracy in determining the base optical path length was estimated to be ±0.25 cm and contributed a negligible amount to the overall uncertainty. Thus, the uncertainty in determining the OH concentration from the factors in equation E1 was estimated to be about ±7% at the 95% confidence level.

As discussed in section III.F, the pulse-to-pulse fluctuations in the initial OH concentration caused less than ±0.5% uncertainty in k_{1a}. The OH concentration gradient also produced only a small influence on the determination of k_{1a}, but this effect is hard to quantify. In section III.F, the simulated OH profile shown in Figure 7a was generated using eq E2 for computational efficiency. However, eq E2 is based on the use of the steady-state approximation to describe the O atom time dependence. Under the conditions of Figure 7, this is only valid at early reaction times. Further, the uncertainty in the determination of the optimized value of k_{1a} by the computer analysis was always of the order of ±5%. Loh and Jasinski[70] and Fahr and Laufer[71] examined the influence of the reactant concentration gradient on the measured rate constant for pure second-order decay and concluded that even for gradients approaching 100%, the error in the rate constant was only 5%. We conclude that the concentration gradient along the photolysis axis had little influence on the determination of k_{1a}.

The propagation of an uncertainty in a specific rate constant in a kinetic model into an uncertainty in a derived rate constant using the model is not straightforward; however, the use of IRCFs does provide a reasonable estimate. If the specific reaction involves a species that directly reacts with a reactant involved in the reaction of interest, the uncertainty in the derived rate constant is related to the uncertainty in the specific rate constant times the ratio of the IRCF for the specific reaction and the IRCF for the reaction of interest. As discussed in section III.E, the most significant reactions contributing to OH removal were reactions 1a, and 2 and diffusion. The reliability of k_2 has been estimated to be about ±25%, at the 95% confidence limit.[18] Typical examples of IRCFs for these processes are shown in Figure 7, and on average, the ratio of IRCF_{O}^{OH} to IRCF_{OH}^{OH} is about 0.35 ± 0.05 depending on the experimental conditions. Thus, the uncertainty in k_{1a} introduced from the uncertainty in k_2 can be calculated to be about ±9%, at the 95% confidence level. Similarly, under the conditions were the determination of k_{1a} was made, diffusion accounted for nearly half the removal of OH (see Figure 6b,c) so that the uncertainty in k_{diff}^{OH} directly resulted in a corresponding uncertainty in k_{1a}. Generally, k_{diff}^{OH} was determined several times in each experiment, and the uncertainty was estimated to be ±10%, at the 95% confidence limit. Thus the uncertainty in k_{diff}^{OH} produced a corresponding uncertainty in k_{1a} of ±10%. As mentioned in section III.C, the time scale over which the OH temporal profiles were fit was varied in a few cases, and on average, the shorter the time scale the smaller the value of k_{1a} and the vice versa. However, this was a small effect and no systematic trend was established.

There is another source of O atoms in the experiment besides reaction 1a, and that is the quenching of $O(^1D)$ to $O(^3P)$ by H_2O, N_2O, and Ar or Ne, reactions 3c, 4c, and 5. The data were analyzed using the rate constants for quenching of $O(^1D)$ listed in Table 1. The uncertainty in the various rate constants are k_{3c} ± 65%, taken to be at the 95% confidence level,[35] k_{4c} ± 100% an upper limit,[36] and k_5 ± 38%, for Ar as a quenching partner at the 95% confidence level.[38] Even at the highest partial pressures, the quenching of $O(^1D)$ by Ne was sufficiently small to contribute only a few percent to the total $O(^3P)$ flux and does not need to be considered. Although the contribution of these individual reactions varied depending on the experimental conditions, a reasonable estimate is given by the following: $\mathrm{IRCF}_{O1D,H_2O}^{O3P} = 0.10$, $\mathrm{IRCF}_{O1D,N_2O}^{O3P} = 0.02$, and $\mathrm{IRCF}_{O1D,Ar}^{O3P} = 0.07$. The propagation of the uncertainties in the $O(^1D)$ quenching rate constants into an uncertainty in the determination of k_{1a} is calculated by propagating the fractional contributions of all the $\mathrm{IRCF}_{O1D,X}^{O3P}$ to the $O(^3P)$ production and OH removal processes. As noted previously, the ratio of IRCF_{O}^{OH} to IRCF_{OH}^{OH} was about 0.35 so that the uncertainty in the determination of k_{1a} due to the uncertainty in the quenching rate constants for $O(^1D)$ was ±6%.

However, there have been new determinations of the rate constants for reactions 3c and 4c that provide different values for these rate constants. For reaction 3, Carl[46] has determined the yield of $O(^3P)$ to be less than 0.003. For reaction 4, there are three new measurements[44,45,46] of the total removal rate and two for the yield[45,46] of O(^{3}P). The weighted average of these new measurements gives the total rate constant for k_4 to be (1.35 ± 0.08) × 10^{-10} cm^3 molecule^{-1} s^{-1} at the 95% confidence limit and the yield of O(^{3}P) to be 0.051 ± 0.01. With these new measurements k_{3c} is 6.6 × 10^{-13} cm^3 molecule^{-1} s^{-1} and k_{4c} is (6.9 ± 0.14) × 10^{-12} cm^3 molecule^{-1} s^{-1}. The contribution of reaction 3c, $\mathrm{IRCF}^{\mathrm{O3P}}_{\mathrm{O1D,H_2O}}$, would decrease to 0.017 and for reaction 4c, $\mathrm{IRCF}^{\mathrm{O3P}}_{\mathrm{O1D,N_2O}}$, would increase to 0.14. Fortunately, the overall production of O(^{3}P) by O(^{1}D) quenching is only increased slightly by this new information. The effect of these new rate constant measurements was tested in a few simulations, and indeed the optimum k_{1a} values were found to be reduced by a few percent. To account for the influence of these new measurements, the contribution of O(^{1}D) quenching to the systematic uncertainty in the determination of k_{1a} was increased from ± 6% to ±9%.

Although the recombination reactions 1b, 11, and 12 could contribute up to a 5% to the removal flux of OH at the highest pressures, most of the experiments were made at lower pressures where their contribution was less than 2%. Thus, they are neglected in the error analysis.

In summary, the main systematic errors that effect the determination of k_{1a} have been analyzed: the OH concentration measurement, ±7%; the rate constant for reaction 2, ±9%; the diffusional rate constant of OH, ±10%, and the quenching rate constants for converting O(^{1}D) to O(^{3}P), ±9%. Assuming a Gaussian distribution for these uncertainties, the systematic uncertainties can be added in quadrature to give a total uncertainty of ±18% in the determination of k_{1a} at the 95% confidence level. Combining with the uncertainty due to scatter in the measurements of ±28% at the 95% confidence level, gives an estimate of ±33% in the overall uncertainty in the measurement of k_{1a}, including random and systematic errors.

IV. Summary and Conclusion

The rate constant for the reaction, OH + OH → O(^{3}P) + H_2O, has been measured via direct concentration measurements of the OH radical using high-resolution diode laser absorption spectroscopy on Λ-doublet resolved rotational transitions of the first OH(2,0) overtone. The OH radical was created by pulsed-laser photolysis of N_2O to create O(^{1}D) atoms, which reacted with H_2O to create the OH radical. The measurements were conducted in two carrier gases, Ne and Ar, to provide different conditions for removal of OH by diffusion and electronic quenching of O(^{1}D), with no difference in the determination of k_{1a}. The results were independent of carrier gas and pressure (see Figure 4), as well. The OH temporal concentration profiles were recorded with high signal-to-noise, greater than 200 for OH concentrations of 1.0 × 10^{13} molecules cm^{-3}. With this high signal-to-noise ratio, the value of k_{1a} could be determined to within an uncertainty of about 10% (at the ±1σ level), neglecting systematic errors, even though k_{1a} accounted for between 30 and 40% removal of the OH radicals (see Figures 3 and 4). Several potential sources of error were explored in section III.F but shown to be negligible.

Separate experiments were carried out with H_2 at low and high concentrations to verify the experimental method (see Figure 5). At low H_2 concentrations, the measured k_{1a} values were in agreement with the different carrier gas results. At high concentrations of H_2, the experiments enabled the OH + H_2 rate constant to be measured. Good agreement was found with recent determinations.

The rate constant, k_{1a}, was measured at three temperatures: (2.7 ± 0.9) × 10^{-12} at 293 ± 2 K; (2.0 ± 0.7) × 10^{-12} at 347 ± 4 K; (2.2 ± 0.7) × 10^{-12} cm^3 molecule^{-1} s^{-1} at 373 ± 3 K, where the uncertainty includes an estimate of both random and systematic errors at the 95% confidence limit. The observed-negative temperature dependence of the rate constant is in agreement with recent experimental measurements[16,17] but is in disagreement with another experimental work.[15] These results seem to confirm that k_{1a} has slight negative temperature dependence near 300 K. The measurements at 293 K reported on here are in good agreement with early work using the ESR technique to measure the OH radical concentration but differ by almost a factor of 2 from other results and the IUPAC recommendation (section III.H). Although within the 95% confidence limit of random and systematic errors, the results of this work and the IUPAC evaluation for k_{1a} just overlap, but this is an unsatisfactory situation. Various sources of error were discussed and evaluated but cannot account for this disagreement. It is noted that the more direct methods of determining the OH concentration, TDLS and ESR appear to give similar results. Further study of this important and unique radical−radical reaction appears necessary.

Acknowledgment. This work was supported by the U.S. Department of Energy, Office of Basic Energy Sciences, Division of Chemical Sciences, Geosciences, and Biosciences (under contract No. W-31-109-ENG-38).

References and Notes

(1) Gardiner, W. C., Jr. *Gas-Phase Combustion Chemistry*; Springer-Verlag: New York, 1999.

(2) Glassmann, I. *Combustion*; Academic Press: Orlando, 1987.

(3) Mass, U.; Warnatz, J. *Combust. Flame* **1988**, *74*, 53.

(4) Pilling, M. J.; Stocker, D. W. *Annu. Rep. Prog. Chem. Set. C* **1999**, *95*, 277.

(5) Del Greco, F. P.; Kaufman, F. *Disc. Faraday Soc.* **1962**, *33*, 128.

(6) Dixon-Lewis, G.; Wilson, W. E.; Westenberg, A. A. *J. Chem. Phys.* **1966**, *44*, 2877.

(7) Wilson, W. E., Jr.; O'Donovan, J. T. *J. Chem. Phys.* **1967**, *47*, 5455.

(8) Breen, J. E.; Glass, G. P. *J. Chem. Phys.* **1970**, *52*, 1082.

(9) Mulcahy, M. F. R.; Smith, R. H. *J. Chem. Phys.* **1971**, *54*, 5215.

(10) Westenberg, A. A.; deHaas, N. *J. Chem. Phys.* **1973**, *58*, 4066.

(11) McKenzie, A.; Mulcahy, M. F. R.; Steven, J. R. *J. Chem. Phys.* **1973**, *59*, 3244.

(12) Clyne, M. A. A.; Down, S. *J. Chem. Soc. Faraday Trans. 2* **1974**, *70*, 253.

(13) Trainor, D. W.; von Rosenberg, C. W., Jr. *J. Chem. Phys.* **1974**, *61*, 1010.

(14) Farquharson, G. K.; Smith, R. H. *Aust. J. Chem.* **1980**, *33*, 1425.

(15) Wagner, G.; Zellner, R. *Ber. Bunsen-Ges. Phys. Chem.* **1981**, *85*, 1122.

(16) Bedjanian, Y.; Le Bras, G.; Poulet, G. *J. Phys. Chem. A* **1999**, *103*, 7017.

(17) Sun, H.; Li, Z. *Chem. Phys. Lett.* **2004**, *399*, 33.

(18) Atkinson, R.; Cox, R. A.; Crowley, J. N.; Hampson, R. F., Jr.; Hynes, R. G.; Jenkin, M. E.; Kerr, J. A.; Rossi, M. J.; Troe, J. *Summary of Evaluated Kinetic and Photochemical Data for Atmospheric Chemistry*, http://www.iupac-kinetic.ch.cam.ac.uk/, web version (February), 2006.

(19) Albers, E. A.; Hoyermann, K.; Wagner, H. G. G.; Wolfrum, J. *Thirteenth Symposium (International) on Combustion*; The Combustion Institute: Pittsburgh, PA, 1971; p 81.

(20) Wooldridge, M. S.; Hanson, R. K.; Bowman, C. T. *Int. J. Chem. Kinet.* **1994**, *26*, 389.

(21) Sutherland, J. W.; Patterson, P. M.; Klemm, R. B. *Twenty-Third Symposium (International) on Combustion*; The Combustion Institute: Pittsburgh, PA, 1990; p 51.

(22) Lifshitz, A.; Michael, J. V. *Twenty-Third Symposium (International) on Combustion*; The Combustion Institute: Pittsburgh, PA, 1990; p 59.

(23) Deyerl, H.-J.; Clements, T. G.; Luong, A. K.; Continetti, R. E. *J. Chem. Phys.* **2001**, *115*, 6931.

(24) Harding, L. B. *J. Chem. Phys.* **1991**, *95*, 8653.

(25) Harding, L. B.; Wagner, A. F. *Twenty-Second Symposium (International) on Combustion*; The Combustion Institute: Pittsburgh, PA, 1988; p 983.

(26) Karkach, S. P.; Osherov, V. I. *J. Chem. Phys.* **1999**, *110*, 11918.

(27) Braunstein, M.; Panfili, R.; Shroll, R.; Bernstein, L. *J. Chem. Phys.* **2005**, *122*, 184307.

(28) He, G.; Tokue, I.; Harding, L. B.; Macdonald, R. G. *J. Phys. Chem. A* **1998**, *102*, 7653.

(29) Gao, Y.; Macdonald, R. G. *J. Phys. Chem. A* **2005**, *109*, 5388.

(30) Coxon, J. A. *Can. J. Phys.* **1980**, *58*, 933.

(31) Maillard, J. P.; Chauville, J.; Mantz, A. W. *J. Mol. Spectrosc.* **1976**, *63*, 120.

(32) Fulle, D.; Hamann, H. F.; Hippler, H.; Troe, J. *J. Chem. Phys.* **1996**, *105*, 1001.

(33) Zellner, R.; Ewig, F.; Paschke, R.; Wagner, G. *J. Phys. Chem.* **1988**, *92*, 4184.

(34) Atkinson, R.; Baulch, D. L.; Cox, R. A.; Crowley, J. N.; Hampson, R. F.; Hynes, R. G.; Jenkin, M. E.; Rossi, M. J.; Troe, J. *Atmos. Chem. Phys.* **2004**, *4*, 1461.

(35) Wine, P. H.; Ravishankara, A. R. *Chem. Phys.* **1982**, *69*, 365.

(36) Atkinson, R.; Baulch, D. L.; Cox, R. A.; Hampson, R. F., Jr.; Kerr, J. A.; Troe, J. *J. Phys. Chem. Ref. Data* **1992**, *21*, 1125.

(37) Heidner, R. F., III; Husain, D. *Int. J. Chem. Kinet.* **1974**, *6*, 77.

(38) Blitz, M. A.; Dillon, T. J.; Heard, D. E.; Pilling, M. J.; Trought, I. D. *Phys. Chem. Chem. Phys.* **2004**, *6*, 2162.

(39) Keyser, L. F. *J. Phys. Chem.* **1988**, *92*, 1193.

(40) Seeley, J. V.; Meads, R. F.; Elrod, M. J.; Molina, M. J. *J. Phys. Chem.* **1996**, *100*, 4026.

(41) Baulch, D. L.; Coobs, C. J.; Cox, R. A.; Esser, C.; Frank, P.; Just, Th.; Kerr, J. A.; Pilling, M. J.; Troe, J.; Walker, R. W.; Warnatz, J. *J. Phys. Chem. Ref. Data* **1992**, *21*, 411.

(42) Fulle, D.; Hamann, H. F.; Hippler, H.; Troe, J. *J. Chem. Phys.* **1998**, *108*, 5391.

(43) Nishida, S.; Takahashi, K.; Matsumi, Y.; Taniguchi, N.; Hayashida, S. *J. Phys. Chem. A* **2004**, *108*, 2451.

(44) Dunlea, E. J.; Ravishankara, A. R. *Phys. Chem. Chem. Phys.* **2004**, *6*, 2152.

(45) Takahashi, K.; Takeuchi, Y.; Matsumi, Y. *Chem. Phys. Lett.* **2005**, *410*, 196.

(46) Carl, S. A. *Phys. Chem. Chem. Phys.* **2005**, *7*, 4051.

(47) Ruscic, B.; Pinzon, R. E.; Morton, M. L.; von Laszevski, G.; Bittner, S. J.; Nijsure, S. G.; Amin, K. A.; Minkoff, M.; Wagner, A. F. *J. Phys. Chem. A* **2004**, *108*, 9979.

(48) Ruscic, B.; Wagner, A. F.; Harding, L. B.; Asher, R. L.; Feller, D.; Dixon, D. A.; Peterson, K. A.; Song, Y.; Qian, X.; Ng, C.-Y.; Liu, J.; Chen, W.; Schwenke, D. W. *J. Phys. Chem. A* **2002**, *106*, 2727.

(49) Domalski, E. S.; Garvin, D.; Wagman, D. D. In *National Bureau of Standards (U.S.) Special Publication*; Hampson, R. F., Garvin, D., Eds.; NBS: Gaithersburg, MD, 1978; Appendix 1, p 513.

(50) Ruscic, B.; Pinzon, R. E.; Morton, M. L.; Srinivasan, N. K.; Su, M.-C.; Sutherland, J. W.; Michael, J. V. *J. Phys. Chem. A* **2006**, *110*, 6592.

(51) Fuller, E. N.; Ensley, K.; Giddings, J. C. *J. Phys. Chem* .**1969**, *73*, 3679.

(52) Reid, R. C.; Prausnitz, J. M.; Poling, B. E. *The Properties of Gases and Liquids*; McGraw-Hill: New York, 1989.

(53) Gao, Y.; Macdonald, R. G. *J. Phys. Chem. A* **2006**, *110*, 977.

(54) Lynch, K. P.; Michael, J. V. *Int. J. Chem. Kinet.* **1978**, *10*, 233.

(55) Kroto, H. W. *Molecular Rotation Spectra*; Dover: New York, 1992.

(56) Nelson, D. D., Jr.; Schiffman, A.; Nesbitt, D. J.; Orlando, J. J.; Burkholder, J. B. *J. Chem. Phys.* **1990**, *93*, 7003.

(57) Holtzclaw, K. W.; Person, J. C.; Green, B. D. *J. Quant. Spectrosc. Radiat. Transfer* **1993**, *49*, 223.

(58) HITRAN2004 edition, http://cfa-www.harvard.edu/hitran/; Rothman, L. S.; Jacquemart, D.; Barbe, A.; Benner, D. C.; Birk, M.; Brown, L. R.; Carleer, M. R.; Chackerian, C., Jr.; Chance, K.; Coudert, L. H.; Dana, V.; Devi, V. M.; Flaud, J.-M.; Gamache, R. R.; Goldman, A.; Hartmann, J.-M.; Jucks, K. W.; Maki, A. G.; Mandin, J.-Y.; Massie, S. T.; Orphal, J.; Perrin, A.; Rinsland, C. P.; Smith, M. A. H.; Tennyson, J.; Tolchenov, R. N.; Toth, R. A.; Auwera, J. V.; Varanasi, P.; Wagner, G. *J. Quant. Spectrosc. Radiat. Transfer* **2004**, *96*, 139.

(59) Sauder, D. G.; Stephenson, J. C.; King, D. S.; Casassa, M. P. *J. Chem. Phys.* **1992**, *97*, 952.

(60) Tanaka, N.; Takayanagi, M.; Hanazaki, I. *Chem. Phys. Lett.* **1996**, *254*, 40.

(61) Smith, I. W. M.; Williams, M. D. *J. Chem. Soc., Faraday Trans. 2* **1985**, *81*, 1849.

(62) Silvente, E.; Richter, R. C.; Hynes, A. J. *J. Chem. Soc., Faraday Trans.* **1997**, *93*, 2821.

(63) Aker, P. M.; Sloan, J. J. *J. Chem. Phys.* **1986**, *85*, 1412.

(64) Orkin, V. L.; Kozlov, S. N.; Poskrebyshev, G. A.; Kurylo, M. J. *J. Phys. Chem. A* **2006**, *110*, 6978.

(65) Warnatz, J.; Maas, U.; Dibble, R. W. *Combustion: Physical and Chemical Fundamentals, Modeling and Simulation, Experiments, Pollution Formation*; Springer: Berlin, 1995.

(66) Tulloch, J. M.; Macpherson, M. T.; Morgan, C. A,; Pilling, M. *J. Phys. Chem.* **1982**, *86*, 3812.

(67) Westenberg, A. A. *J. Chem. Phys.* **1965**, *43*, 1544.

(68) Poirier, R. V.; Carr, R. W., Jr. *J. Phys. Chem.* **1971**, *75*, 1593.

(69) Schiffman, A.; Nesbitt, D. J. *J. Chem. Phys.* **1994**, *100*, 2677.

(70) Loh, S. K.; Jasinski, J. M. *J. Chem. Phys.* **1991**, *95*, 4914.

(71) Fahr, A.; Laufer, A. H. *Int. J. Chem. Kinet.* **1993**, *25*, 1029.